JOURNAL OF GEOPHYSICAL RESEARCH: SPACE PHYSICS, VOL. 118, 5659–5672, doi:10.1002/jgra.50545, 2013

Energy transfer and flow in the solar wind-magnetosphere-ionosphere system: A new coupling function

P. Tenfjord[1,2] and N. Østgaard[1,2]

Received 23 April 2013; revised 5 August 2013; accepted 31 August 2013; published 16 September 2013.

[1] In this paper we describe and quantify the energy transfer, flow, and distribution. Our high-resolution data set covers 13 years of OMNI, SuperMAG, and Kyoto data. We employ what we consider to be the best estimates for energy sinks and relate these to SuperMAG indices for better coverage and spatial resolution. For the energy input, we have used the method of dimensional analysis that is presented in unit power and makes it appropriate for energy analysis. A cross-correlation analysis parameterizes the magnetospheric response on the solar wind parameters during a wide range of conditions, ranging from substorms and storms up to a decade. The determined functional form is then evaluated and scaled using superposed epoch analysis of geomagnetic storms, revealing that the effective area of interaction cannot be considered static. Instead, we present a dynamic area which depends to the first order on the cube of the interplanetary magnetic field B_Z component. Also, we find that for longer time periods, this area must be increased compared to the area used for geomagnetic storms. We argue that some of the terms in the energy coupling function are contributory to describing magnetosheath conditions and discuss how our coupling function can be related to Maxwell stress components. Also, we quantify the relative importance of the different energy sinks during substorms, geomagnetic storms, and long time series and present the coupling efficiency of the solar wind. Our energy coupling functions are compared with the ϵ parameter and perform better for almost any event.

Citation: Tenfjord, P., and N. Østgaard (2013), Energy transfer and flow in the solar wind-magnetosphere-ionosphere system: A new coupling function, *J. Geophys. Res. Space Physics*, *118*, 5659–5672, doi:10.1002/jgra.50545.

1. Introduction

[2] The solar wind is the ultimate source of energy and is responsible for virtually all the magnetospheric dynamics. Describing and quantifying the solar wind energy transfer to the Earth's magnetosphere is one of the fundamental questions in space physics. It is well accepted that the energy transfer is closely related to the B_z component of the interplanetary magnetic field (IMF), and through a large-scale reconnection process on the dayside, a small fraction of the available solar wind energy is able to penetrate our magnetosphere [*Dungey*, 1961]. However, this tiny fraction of energy fuels almost all the dynamical processes in the near-Earth space. An enhanced understanding of how the solar wind energy couples with the magnetosphere is an essential part of creating a reliable prediction of the space weather. Our modern society has become increasingly dependent on reliable technology, such as communication, navigation, and electrical power systems, which can be vulnerable to the solar winds influence.

[3] The most important forms of ionospheric and magnetospheric energy dissipation are Joule heating of the ionosphere (U_J), ring current injection (U_R), and particle precipitation (U_A) [*Akasofu*, 1981; *Gonzalez and Gonzalez*, 1984; *Østgaard et al.*, 2002a; *Turner et al.*, 2009]. The energy deposited into these sinks can be estimated using ground-based magnetometer data [*Dessler and Parker*, 1959; *Sckopke*, 1966; *Akasofu*, 1981; *Ahn et al.*, 1983]. Energy dissipated through minor ionospheric channels, e.g., ion outflow and auroral kilometric radiation, and magnetospheric energy dissipation processes such as plasmoid ejection and plasma sheet heating are neglected, because they are small or not part of the closed magnetospheric system of interest (e.g., plasmoid) [*Koskinen and Tanskanen*, 2002; *Baker et al.*, 1997; *Knipp et al.*, 1998; *Ieda et al.*, 1998]. There is no direct method of monitoring the energy transferred to the magnetosphere by the solar wind. The local energy conversion across the magnetopause has been estimated with Cluster; however, this is restricted both in spatial and temporal resolution [see *Rosenqvist et al.*, 2006, 2008; *Anekallu et al.*, 2011]. Instead, one estimates the energy needed to drive the magnetospheric system using ionospheric and magnetospheric indices as proxies. The

[1]Birkeland Centre for Space Science, Bergen, Norway.
[2]Department of Physics and Technology, University of Bergen, Bergen, Norway.

Corresponding author: P. Tenfjord, Department of Physics and Technology, University of Bergen, Allegt 55, Bergen NO-5007, Norway. (paul.tenfjord@ift.uib.no)

2169-9380/13/10.1002/jgra.50545

so-called coupling function is then related to upstream solar wind parameters and evaluated in terms of the correlation with estimated energy dissipative processes in the ionosphere and inner magnetosphere.

[4] The most widely used energy coupling function is the ϵ parameter by *Akasofu and Perreault* [1978]. The ϵ parameter is a semiempirical parameter representing the energy input rate (W, J/s). The parameter was parameterized by assuming that the energy required to power the magnetosphere-ionosphere system is provided by the solar wind. The required energy is a measure of the total rate of energy dissipation in the inner magnetosphere and ionosphere. The ϵ parameter is given in SI units as [*Koskinen and Tanskanen*, 2002]

$$\epsilon\,[\mathrm{W}] = \frac{4\pi}{\mu_0} VB^2 \sin^4(\theta/2) l_0^2 \tag{1}$$

where V,B,θ, and l_0 are the solar wind velocity, total magnetic field, clock angle, and the effective area of interaction, respectively. The clock angle is the angle between the IMF vector projected into the GSM $Y - Z$ plane and the Z axis, positive in the clockwise direction as seen from the Sun. The ϵ parameter is often interpreted as to be derived from the Poynting flux.

[5] A more general expression for the reconnection power was presented by *Gonzalez and Mozer* [1974], where the authors explained the energy transfer as the Joule heating rate of the reconnection-electric field and the magnetopause current. In a comparison by *Gonzalez and Gonzalez* [1984] between the ϵ parameter and the more general expression [*Gonzalez and Mozer*, 1974], the authors showed that for the limit that involves equal geomagnetic and magnetosheath magnetic field amplitudes, their functional form reduces to that of the ϵ parameter.

[6] In recent years, several coupling functions have been proposed by numerous authors (see *Gonzalez et al.* [1994] or *Newell et al.* [2007] for a review), attempting to parameterize the magnetospheric response to solar wind driving more accurately. Perhaps the main reason why the ϵ parameter is the most widely used is that it quantifies the energy transfer in terms of power (W), and the time-integrated values (J) can be compared to estimated energy sinks in the ionosphere and inner magnetosphere. Also, the ϵ parameter is to our knowledge the only energy coupling function which is scaled to the magnetospheric energy sinks.

[7] Even though *Akasofu* [1981] made it clear that the ϵ parameter should be considered as a first approximation, it has without doubt played a crucial part of our general understanding of solar wind-magnetosphere-ionospheric interaction, as will be outlined below. The ϵ parameter was originally scaled to geomagnetic storm events; however, it has been used to study a wide range of time scales and conditions.

[8] *Stamper et al.* [1999] studied century-long coupling between geomagnetic activity and solar wind in search for mechanisms responsible for long-term increase in geomagnetic activity. *Knipp et al.* [1998] presented an event-specific origin-to-end view of an geomagnetic storm event. While *Kallio et al.* [2000] used the ϵ parameter to study the loading-unloading processes during substorms, *Tanskanen et al.* [2002] analyzed the substorm energy budget during low and high solar activities. *Lu et al.* [1998] used the ϵ parameter to quantify the global magnetospheric energy deposition during a magnetic cloud event. *Palmroth et al.* [2010] studied the magnetospheric feedback in the energy transfer process and, using the Grand Unified Magnetosphere Ionosphere Coupling Simulation, version 4 (GUMICS-4), found that the energy transfer can continue even after the direct driving conditions turned unfavorable. This was termed as hysteresis effect. *Koskinen and Tanskanen* [2002] addressed the underlaying physical foundation for the ϵ parameter and clarified how the parameter should be interpreted and used.

[9] In the last 30 years, the data and our understanding of the dissipative processes in the inner magnetosphere and ionosphere have been greatly improved, and it has been generally accepted that the scaling factor, l_0, in the ϵ parameter is somewhat low [*Østgaard et al.*, 2002b; *Koskinen and Tanskanen*, 2002].

[10] The purpose of this paper is to derive an energy coupling function that is valid for a wide range of solar wind conditions and time scales, ranging from substorms and storms, up to a decade. We will require the function to balance the energy sinks in the ionosphere and inner magnetosphere with the estimated magnitude much improved since the ϵ parameter was derived. By letting the effective area of energy transfer be a free parameter, we will optimize the coupling function to be valid for long time series. This new and dynamic energy coupling function will then be discussed in terms of Maxwell stress and magnetosheath conditions in order to gain a better understanding of how the flow of energy is transferred from the solar wind to the magnetosphere.

2. Theoretical Background

2.1. Energy Source and Sinks

[11] In this section we introduce the energy source and sinks in the solar wind-magnetosphere-ionosphere system.

2.1.1. Solar Wind Kinetic Energy

[12] The solar wind is the ultimate source of energy in the system. The kinetic energy flux of the solar wind available for the magnetosphere is

$$U_{SW} = \frac{1}{2}\rho V_x^3 A \tag{2}$$

where A is the cross-sectional area of the magnetosphere, assuming cylindrical symmetric configuration, and V_x is the x component of the solar wind velocity. Magnetic and thermal energies in the solar wind are usually 1 or 2 orders of magnitude smaller than kinetic energy and are neglected for this reason.

[13] To estimate A, we use the empirical model of the near-Earth magnetotail geometry by *Petrinec and Russell* [1996]. Using this model, we calculate the magnetotail radius, R_T, for a given nightside position of $X_{\mathrm{GSM}} = -30\,R_E$. Entering this into equation (2), the available solar wind kinetic energy flux is estimated.

2.1.2. Joule Heating

[14] Joule heating is caused by ionospheric currents which heat the atmosphere and takes place through the Pedersen currents associated with the closure of field aligned currents in the resistive ionosphere [*Koskinen and Tanskanen*, 2002]. The mechanism can be recognized as Ohmic

dissipation: loss of electric energy when a current flows through a resistive medium, where the work done on the particles will increase their mechanical energy. *Vasyliunas* [2005] argues that Joule heating is not primarily Ohmic or Joule heating in the physical sense, rather simply frictional heating from the relative motion of plasma and neutrals [*Song et al.*, 2009].

[15] Joule heating can be estimated using various methods and techniques and has been studied using experimental data [*Ahn et al.*, 1983, 1989; *Baumjohann and Kamide*, 1984; *Richmond et al.*, 1990], large statistical studies [*Foster et al.*, 1983], assimilative data methods (assimilative mapping of ionospheric electrodynamics (AMIE)) [*Lu et al.*, 1998], and global MHD simulations [*Palmroth et al.*, 2004]. There is a dispute in the community about the actual contribution of Joule heating [*Vasyliunas*, 2005], and the different techniques give contradictory results [*Palmroth et al.*, 2006]. Among the experimental results, the estimates differ by approximately a factor 2, while the MHD results deviate by more than a factor 10. A thorough assessment of Joule heating can be found in *Palmroth et al.* [2005].

[16] In this paper we use results from experimental studies and estimate the Joule heating rate using the auroral electrojet (*AE*) index as a proxy. *Østgaard et al.* [2002b] reviewed several results, and we adapt their conclusion for the reasons given there. In their paper the results from *Ahn et al.* [1989] (summer) and *Richmond et al.* [1990] (winter) were used. The Joule heating in both hemispheres during solstice is then given by

$$U_J\,[\mathrm{GW}] = 0.54AE + 1.8 \tag{3}$$

We relate Joule heating rate to the SuperMAG indices instead of *AE*, by determining an average value of the ratio SuperMag electrojet (*SME*)/*AE* during several periods when the Kyoto AE magnetometers were well located. We simply use the ratio to rewrite equation (3) and express the Joule heating rate as a function of *SME*:

$$U_J\,[\mathrm{GW}] = 0.48SME \tag{4}$$

We notice that the values of Joule heating have a seasonal dependence [see *Østgaard et al.*, 2002b, Table 2], so our solstice values may not be valid for all seasons. *Ahn et al.* [1983] suggested $U_J = 0.23AE$ (one hemisphere) during equinox; this implies a seasonal difference from solstice to equinox of $\sim$ 15%. We will discuss how other choices of U_J would affect our results in section 7.

2.1.3. Auroral Precipitation

[17] Particles with their mirror point below 100 km are very likely to deposit their energy through ionization, aurora, and heating, due to increased density of neutral particles below this height. By deriving the electron energy deposition (0.1–100 keV) from UV and X-ray emissions in the Northern Hemisphere, *Østgaard et al.* [2002a] found the relation between *AL* index and energy deposited to be

$$U_A\,[\mathrm{GW}] = 4.4 \cdot AL_{QL}^{1/2} - 7.6 \tag{5}$$

Østgaard et al. [2002a] used data derived from UV and X-ray emission during seven isolated substorms verified using DMSP data [*Østgaard et al.*, 2001] and Kyoto Quicklook indices (six to eight stations). During two of these substorms, the stations available were poorly located. Therefore, only five substorms were used in their analysis.

[18] By using the same data set as *Østgaard et al.* [2002a], with final Kyoto indices (12 stations) and seven substorms, the same analysis has been performed and a slightly different relation, which is valid for AL_{final}, is given as $U_A = 4.3AL^{1/2} - 9$.

[19] We rewrite U_A to be a function of the SuperMAG lower (*SML*) index by the same method as used for Joule heating:

$$U_A\,[\mathrm{GW}] = 4.1 \cdot \sqrt{SML} - 9 \tag{6}$$

We acknowledge that the method used to rewrite the Joule heating rate and particle precipitation to be functions of SuperMAG may seem brutal; however, in our opinion, the advantage of superior coverage and spatial resolution in SuperMAG exceeds the rough estimate. U_A may also have a seasonal dependence which is unknown [see *Barth et al.*, 2004; *Newell et al.*, 1996]. This will be discussed in section 7.

2.1.4. Ring Current Injection

[20] Via the so-called Dessler-Parker-Schopke (DPS) relation [*Dessler and Parker*, 1959; *Sckopke*, 1966], the *Dst* index can be used to estimate the energy increase of the ring current. During disturbed solar wind conditions, variations in the solar wind pressure modulate currents flowing at the dayside magnetopause [*Gonzalez et al.*, 1994]. The magnetosphere is compressed by the sudden increase in solar wind dynamic pressure and at the same time the eastward magnetopause current intensifies. This is observed as an increase in the *Dst* index. However, this is not related to the ring current and we therefore remove this effect by using the pressure-corrected *Dst* index:

$$Dst^* = Dst - \Delta H \tag{7}$$

By adopting the analysis by *Østgaard et al.* [2002b], we use the following equation for the pressure correction [*Gonzalez et al.*, 1994; *Prigancová and Feldstein*, 1992]:

$$\Delta H\,[\mathrm{nT}] = 5 \times 10^5 (\mathrm{nT\,(J\,m^{-3})^{-1/2}}) \cdot P_f^{1/2} - 20\,\mathrm{nT} \tag{8}$$

where P_f is the solar wind dynamic pressure given in pascal.

$$U_R\,[\mathrm{GW}] = -4 \times 10^4 \left(\frac{\partial Dst^*}{\partial t} + \frac{Dst^*}{\tau} \right) \tag{9}$$

with the ring current decay rate given as τ = 4, 8 or 20 h for $Dst^* < -50$, < -30, and > -30 nT, respectively. We have adopted the values from *Lu et al.* [1998] but will discuss the effect of using a dynamic τ value as proposed by *O'Brien and McPherron* [2000].

[21] We have used the *SYM-H* index which we consider to be the equivalent high-resolution version of the *Dst* index [*Wanliss and Showalter*, 2006]. The SuperMAG *SMR* index [*Newell and Gjerloev*, 2012] was also considered; however, due to its generally higher values, this resulted in an underestimate of the loss term in equation (9).

[22] The total energy dissipation rate is defined as the sum of particle precipitation, Joule heating, and ring current injection:

$$U_T = U_A + U_J + U_R \tag{10}$$

2.2. Energy Coupling Between the Solar Wind and Magnetosphere

[23] Electric field related coupling functions [e.g., *Sonnerup*, 1974; *Burton et al.*, 1975; *Kan and Lee*, 1979;

Newell et al., 2007; *Borovsky*, 2008; *Milan et al.*, 2012] generally express the reconnection electric field, or the rate at which magnetic flux is opened at the magnetopause. From an energy perspective, the reconnection rate is a measure of field lines added to the magnetotail. The energy density associated with a magnetic field is also the magnetic pressure given by $B^2/2\mu_0$ [Pa, J/m^3]. Thus, the product $VB^2/2\mu_0$ represents the flow of magnetic energy, or rate at which the energy contained in the field lines is transported through the magnetopause (energy flux density through unit area). The energy transfer rate of solar wind to the magnetosphere is generally explained from an electrodynamical view, by using the Poynting flux to relate the concept of energy to the fields. The energy transfer is then described as the amount of Poynting flux admitted into the magnetosphere. Thus, the conservation of energy is established by means of the Poynting theorem, which states that the power delivered into the magnetospheric volume from electromagnetic fields is equal to the Joule heating in the volume plus the increase in the energy stored in the fields in the volume. In this view, the energy transfer process can be expressed in terms of the familiar laws of electric circuit theory. The dynamics can then be understood in terms of Joule heating at the magnetopause (generator) [*Gonzalez and Mozer*, 1974], inductance of the magnetic fields in the tail, and the ionosphere as the resistor (load). Qualitatively, the entire high-latitude boundary is a generator ($\vec{E} \cdot \vec{J} < 0$) [*Koskinen and Tanskanen*, 2002; *Yeh et al.*, 1981]. The Poynting vector can be written as $\vec{S} = (-\vec{v} \times \vec{B}) \times \vec{B}/\mu_0 = \vec{v_\perp} B^2/\mu_0$. Describing the energy transfer via the Poynting flux is without doubt the most convenient way, it also allows the use of the familiar laws of electrodynamics; however, $\vec{E}$ and $\vec{J}$ are derived from $\vec{v}$ and $\vec{B}$ and do not control the dynamics [*Parker*, 2007]. Channeling upstream Poynting flux from the solar wind to the magnetosphere does not provide an adequate description of the transfer processes, as the bow shock and magnetosphere are actually sources of Poynting flux. Also, in the reference frame of the plasma, the Poynting vector vanishes; the correct description of the energy transfer should be valid in any frame of reference.

[24] It has become generally accepted that the correct description of the energy transfer [*Rosenqvist et al.*, 2006; *Koskinen and Tanskanen*, 2002] is via the Maxwell magnetic stress tensor [*Siscoe and Cummings*, 1969; *Siscoe and Crooker*, 1974]. The quantitative formulation was given by *Siscoe and Cummings* [1969]. The general description is based on the conservation of momentum. The conservation of momentum equation, which is a consequence of Newton's second law of motion, states that the rate of change of momentum in a differential volume is equal to the total force acting on it. In ideal magnetohydrodynamics (MHD), the magnetic field is obliged to move with the plasma; thus, the plasma experiences the magnetic stresses. The MHD momentum equation can be written as [cf. *Siscoe and Siebert*, 2006; *Siscoe*, 1972; *Parker*, 2007]

$$\frac{\rho \partial v_j}{\partial t} = -\left(\frac{\rho v_i \partial v_j}{\partial x_i} + \frac{\partial p_{ij}}{\partial x_i} - \frac{\partial M_{ij}}{\partial x_i} \right) \tag{11}$$

or

$$F_j = \oint -R_{ij} - p_{ij} + M_{ij} \cdot n_i \mathrm{d}\sigma \tag{12}$$

where the divergence theorem has been used to convert equation (11) to an area integral (equation (12)), ρ is the mass density, $M_{ij} = -\delta_{ij} \frac{B^2}{2\mu_0} + \frac{B_i B_j}{\mu_0}$ is the Maxwell magnetic stress tensor, $R_{ij} = \rho v_i v_j$ is the Reynolds stress (momentum flux density transported by the mean bulk velocity), and p_{ij} is the thermal pressure tensor (momentum flux density transported by the thermal motions). The physical meaning of *ij* could be referred to as the force acting in the *j*th direction on a surface that is oriented perpendicular to the *i*th direction. In equation (12), the right-hand side is the closed surface integral over the momentum stress tensor. The left-hand side represents the total acceleration of the mass, hence, the force on the magnetosphere [*Siscoe and Siebert*, 2006]. The forces acting perpendicular to the surface are called normal stresses and forces acting tangential to the surface tangential stresses. *Siscoe* [1972] argues that only tangential stresses result in energy transfer, since a tangential force acts against the solar wind flow. Thus, in the absence of tangential forces at the tail boundary, the forces are always perpendicular to the solar wind flow and no energy is extracted. Tangential stresses are associated with viscous (e.g., Kelvin-Helmholtz instability) and electromagnetic (electric and magnetic) stresses. The momentum transport from thermal motions is assumed to play no significant role [*Vasyliunas et al.*, 1982]. The Reynolds stress is also neglected; the diagonal terms are neglected from our assumption that the solar wind flows parallel to the tail boundary. The shear components that arise from turbulent fluctuations on the mean flow, which can be associated with eddy viscosity [*Borovsky and Funsten*, 2003], are significant when studying viscous-related momentum transfer but here considered small compared to electromagnetic stresses. Thus, considering only electromagnetic forces (we neglect electric stresses because it is small [*Siscoe*, 1972]), the total force can be expressed as the magnetic surface stress:

$$F_j = \oint M_{ij} n_i \mathrm{d}\sigma = \oint \frac{1}{\mu_0} \left(B_i B_j - \frac{1}{2} \delta_{ij} B^2 \right) \cdot n_i \mathrm{d}\sigma \tag{13}$$

The diagonal terms in equation (13) represent magnetic pressure, and the off-diagonal elements are shears. We define the shear stress in the Maxwell stress tensor ($i \neq j$ in equation (13)) in cylindrical coordinates as

$$F_t = \frac{1}{\mu_0} B_n B_t \tag{14}$$

where F_t denotes the tangential force and B_n and B_t are the normal and tangential components of the magnetic field at the magnetopause. The power delivered to the field can then be expressed as [cf. *Siscoe and Cummings*, 1969; *Siscoe and Crooker*, 1974; *Vasyliunas et al.*, 1982]

$$P = \oint \frac{B_n \vec{B}_t \cdot \vec{V}}{\mu_0} \mathrm{d}\sigma \tag{15}$$

where $\vec{V}$ is the plasma flow (assumed equal to upstream solar wind velocity) and the integral is taken over the surface of the magnetotail. The main mechanism which results in tangential magnetic stress on the tail boundary is magnetic reconnection. When the IMF merges with the terrestrial magnetic field at the subsolar point, the stress in the field lines attempts to straighten the field lines and accelerate the plasma. Behind the terminator plane (approximately), the

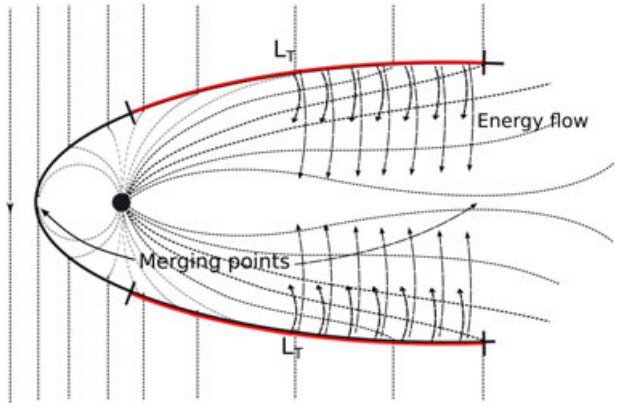

Figure 1. Sketch showing the magnetosphere with magnetic field lines in merging configuration. The energy flow pattern is shown as blurry lines indicating energy transfer from the tail boundary. The distance L_T is measured from the beginning of solar wind-retarding forces and limited by the boundary where the energy flow line intersects the merging point (NENL). Adopted from *Siscoe and Crooker* [1974].

magnetic field slows down the solar wind plasma as the field lines are stretched tailward. This region we define as the transfer region, L_T, and we consider the energy extraction to be limited by the start of solar wind-retarding forces and the intersection with the boundary of the energy flux line that connects to the merging point in the neutral sheet [*Siscoe and Crooker*, 1974], see Figure 1. This is approximately beyond the cusp region to the position where the near-Earth neutral line (NENL) is located.

[25] There are no direct method to measure the total rate at which energy is extracted from the solar wind by the magnetosphere and no obvious theoretical method to calculate B_n and B_t (see equation (15)) from first principles (this will be discussed further in section 7). Rather, we employ a semiempirical analysis using the dimensional analysis introduced by *Vasyliunas et al.* [1982], intending to express the dimension of a quantity as a product of the basic fundamental dimensions. We cross-correlate solar wind parameters to the estimated energy sinks and use the constraints imposed by the dimensional analysis as a template to parameterize a general formula expressing the rate of solar wind-magnetosphere energy transfer [*Vasyliunas et al.*, 1982]. The general expression for the rate of energy transfer, involving only MHD flow and by assuming that the Chapman-Ferraro length remains constant at the magnetopause [*Gonzalez*, 1991], can be expressed as [*Vasyliunas et al.*, 1982]

$$P_V = \rho V^3 l_{CF}^2 M_A^{2\alpha} F(\theta) = \frac{\rho^{1-\alpha} V^{3-2\alpha} B_T^{2\alpha}}{\mu_0^{\alpha}} l_{CF}^2 F(\theta) \qquad (16)$$

where ρ is the solar wind density, V the solar wind velocity, and B_T is the transverse interplanetary magnetic field (IMF) defined as $B_T = \sqrt{B_y^2 + B_z^2}$. The Alfvén Mach number, based on the transverse magnetic field, can be expressed as

$$M_A = \frac{v}{v_A} = \frac{\sqrt{\mu_0 P_f}}{B_T} \qquad (17)$$

where v_A is the Alfvén velocity. The angular dependence, $F(\theta)$, represents the reconnection efficiency from zero, when the IMF is parallel to the magnetopause field, to maximum as the IMF rotates to being antiparallel. A separate analysis, not presented in the paper, showed that the correlation was not strongly dependent on the exponent used in the term $\sin^{\beta}(\theta/2)$. Overall we found, based on trials, that $F(\theta) = \sin^4(\theta/2)$ performed better than the alternatives ($\beta = 1, 2, 3, 5$). This will be discussed in section 7. The physical interpretation of $\beta = 4$ is that only the dawn-dusk component of the reconnection electric field contributes to the energy transfer [*Gonzalez and Mozer*, 1974; *Kan et al.*, 1980; *Gonzalez and Gonzalez*, 1981]. In comparison, *Newell et al.* [2008] used $\beta = 8/3$ while *Milan et al.* [2012] found the best correlation when $\beta = 4.5$.

3. Instrumentation and Data Processing

[26] We have employed the OMNI data set for solar wind measurements. OMNI (available from NASA's Space Physics Data Facility, http://omniweb.gsfc.nasa.gov/) is a multispacecraft (ACE, Wind, Geotail, IMP 8) compilation of near-Earth, high-resolution solar wind magnetic field and plasma data, shifted to Earth's bow shock nose using a minimal variance technique [*Weimer et al.*, 2003]. It also contains geomagnetic activity indices (*Kp, SYM-H, AE*), sunspot number, and additional computed parameters such as plasma flow pressure, plasma beta, Alfvén Mach number, and electric field [*King and Papitashvili*, 2005]. We use 5 min resolution and the data set covers a period from January 1997 to January 2010.

[27] In addition to the indices that are included in the OMNI data, we also use *SME* and *SML*. These magnetic indices are derived from the magnetometer data provided by the SuperMAG collaborators [*Gjerloev*, 2012; *Newell and Gjerloev*, 2011a, 2011b]. SuperMAG (http://supermag.uib.no) is a worldwide collaboration of organizations and national agencies that currently operate more than 300 ground-based magnetometers.

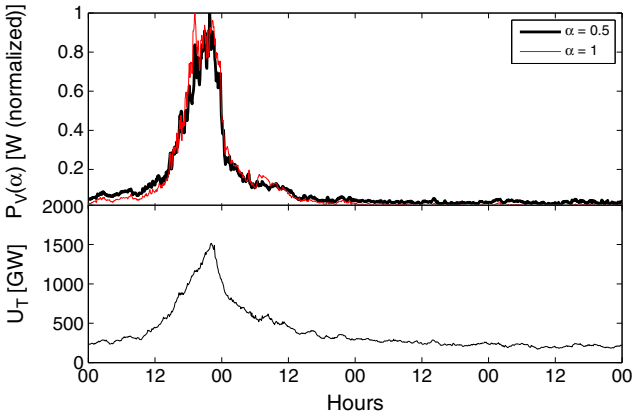

Figure 2. (top) P_V (given in equation (16)) for two different values of the dimensionless numerical parameter α. (bottom) The total energy dissipation U_T (time shifted 30 min according to the cross correlation) during the superposed epoch events.

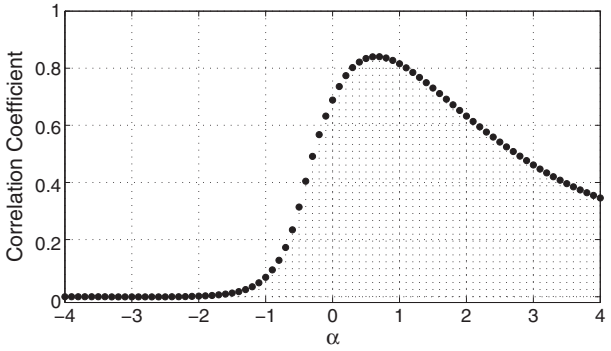

Figure 3. Superposed correlation analysis between $P_V(\alpha)$ and the total energy sinks, U_T, based on the average values from the 45 geomagnetic storms. The maximum correlation, $R = 0.84$, is found at $\alpha \approx 0.5$.

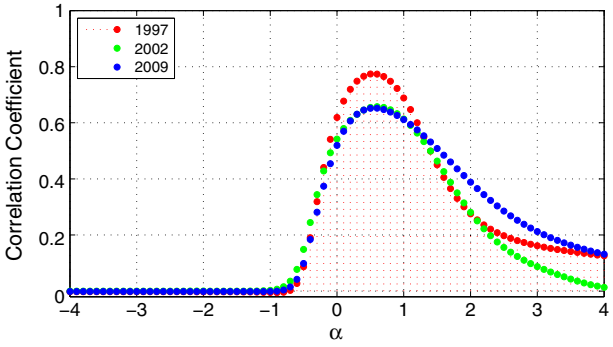

Figure 4. Correlation analysis between $P_V(\alpha)$ and the total energy sinks, U_T for three different periods. The correlation coefficient has its maximum when the dimensionless numerical parameter $\alpha \approx 0.5$. Approximately, 4% of the OMNI solar wind data have been linearly interpolated to compute the correlation.

4. Events and Methodology

[28] We have identified 45 isolated geomagnetic storms where 7 of these are severe. A geomagnetic storm is defined "as an interval of time when a sufficiently intense and long-lasting interplanetary convection electric field leads, through a substantial energization in the magnetosphere-ionosphere system, to an intensified ring current strong enough to exceed some key threshold of the quantifying storm time *Dst* index" [*Gonzalez et al.*, 1994]. These are identified based on a criterion that there are no other storms 3 days prior to the event and no new storms during the recovery phase. Using these storms, we create an averaged storm which we define to last 4 days. We have chosen to align the data using the minimum *SYM-H* values as the common incident. The duration of the storm is defined to 1 day prior to the minimum value of *SYM-H*, interpreted as energy-loading phase, and 3 days after representing energy-unloading phase. In order to analyze the energy flow for a wide range of conditions, we have also identified 29 isolated substorms and several long time periods with consistent solar wind data. For the long time periods, we present three intervals: 20 days, 4 months, and our whole data set 13 years.

[29] In order to determine the functional form of the energy coupling function, we perform a cross-correlation analysis between the total energy sinks (U_T) in our system and P_V with $F(\theta) = \sin^4(\theta/2)$ using the data set described. Given such a determination, we can analyze the amount of energy transferred and deposited to the inner magnetosphere and ionosphere by integrating the energy coupling function and estimated sinks over a period of time. This allows us to scale the effective area of interaction such that the energy is balanced in the system. We also perform an analysis of how the coupling function performs during a wide range of conditions and time scales, again letting the effective area be a free parameter.

5. Correlation Analysis

5.1. General Energy Transfer Formula

[30] Using equation (16) with $F(\theta) = \sin^4(\theta/2)$, constant area ($l_{CF}$ = const.), and allowing α to vary between –4 and 4, a cross-correlation analysis between the energy sinks, U_T and $P_V(\alpha)$, is performed. We allow both α and the time shift to vary to maximize the correlation coefficient. In terms of illustrating the method, Figure 2 shows P_V (equation (16)) for α equal to 0.5 and 1 and the total energy dissipation $U_T = U_R + U_J + U_A$ for the superposed geomagnetic storms. We note that when $\alpha = 1$, the resulting functional form is the (transverse) ϵ parameter based on B_T.

5.2. Geomagnetic Storms

[31] We perform the correlation analysis based on the geomagnetic storm events between $P_V(\alpha)$ and U_T. For each storm, the entire storm interval is used to estimate correlation between $P_V(\alpha)$ and U_T for various values of α, and the average coefficient for the 45 storms is plotted for a given α. Figure 3 shows the result, the x axis represents the dimensionless numerical parameter α in equation (16), and the y axis represents the correlation coefficient. We found the maximum correlation, $R = 0.84$, when $\alpha \approx 0.5$. The energy sinks are time shifted on average $\approx$ 30 min. We also considered separate shifts for the U_R compared to U_A and U_J. However, since the pressure corrected *SYM-H* inside U_R

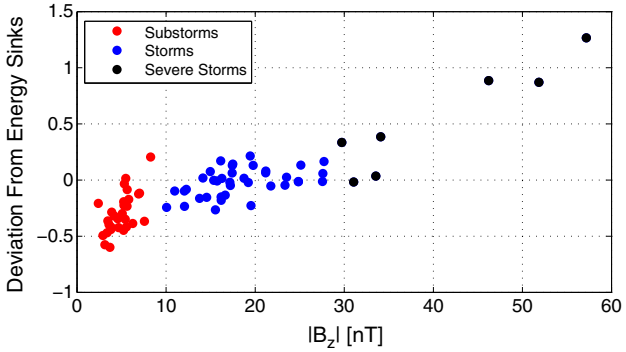

Figure 5. Scatterplot between the deviation from energy sinks and the absolute magnitude of the B_z component which has been averaged 30 min during maximum solar wind driving. The energy input is underestimated for substorm events (red), the energy is balanced for minor to intermediate storms (blue), and the energy input is overestimated for severe storms (black).

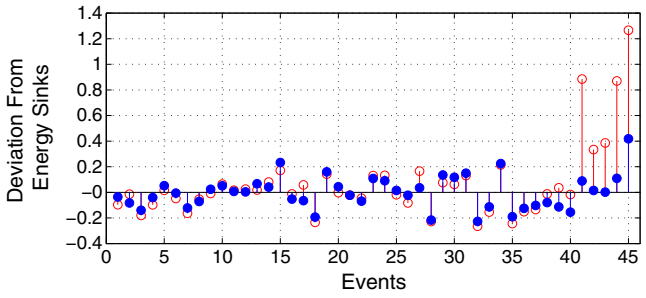

Figure 6. Deviation of the integrated energy input coupling function from the integrated energy sinks for geomagnetic storms. Blue filled points represent the energy coupling function with a dynamic effective area of interaction, while open red points are for a static effective area of 126 R_E^2. The standard deviation (mean deviation) is 0.13 (0.10) and 0.29 (0.18) for the blue and red points, respectively.

often will begin to decline prior to the original *SYM-H*, the effect of separate shifts minimizes.

5.3. Long Time Series

[32] Figure 4 shows the correlation analysis for three different years. Even though the shape of the curves differs, the maximum correlation is found at $\alpha \approx 0.5$. The functional form with best correlation during both geomagnetic storms and long time series is then

$$P_{input}(\alpha = 0.5) = \frac{P_f^{1/2} V_x B_T}{\mu_0^{1/2}} 2L_M L_T \sin^4(\theta/2)$$
$$= \frac{B_T^2 V_x}{\mu_0} M_A \sin^4(\theta/2) 2L_M L_T \qquad (18)$$

where we have used V_x instead of V, and $2L_M L_T$ instead of l_{CF}, the former due to higher correlation coefficient while the latter was done by the assumption that the effective area of interaction is a product of the merging length on the dayside and a transfer region on the tail boundary [*Siscoe and Crooker*, 1974; *Kan and Akasofu*, 1982; *Gonzalez*, 1990].

5.4. Effective Area of Interaction

[33] To determine the effective area of interaction $2L_M L_T$, we scale P_{input} to the energy sinks in the system and require that

$$\int_{t1}^{t2} P_{\text{input}} \mathrm{d}t = \int_{t1}^{t2} P_{\text{output}} \mathrm{d}t = W(P)\,[\text{J}] = W(U_T)\,[\text{J}] \qquad (19)$$

where we use $(2 \cdot L_M \cdot L_T)$ as a scaling factor.

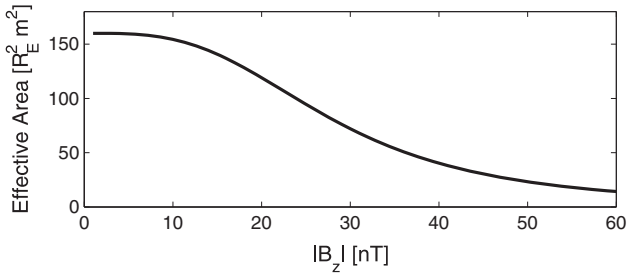

Figure 7. Function $G(B_z)$ (equation (24)) describing the dynamic effective area of interaction.

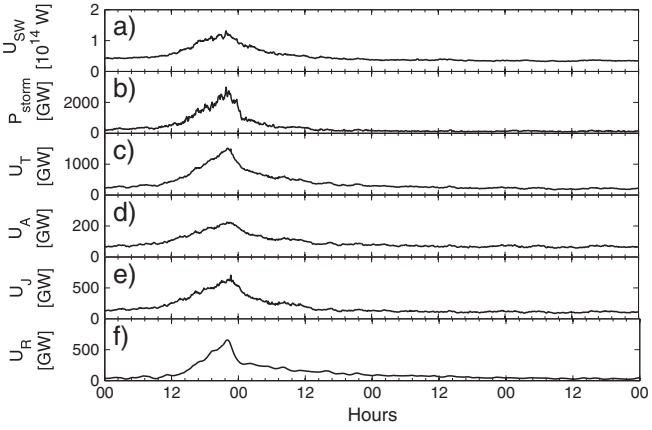

Figure 8. Energy available and transferred from the solar wind and the various energy dissipations into the inner magnetosphere and ionosphere. (a) Available solar wind kinetic energy. (b) Energy coupling function P_{storm} given in equation (23). (c) The total energy dissipated. (d) Global energy deposition by electron precipitation. (e) Joule heating of the ionosphere. (f) The ring current injection rate.

[34] The total output is the time-integrated energy sinks in the system:

$$W(U_T)\,[\text{J}] = \int_{t1}^{t2} U_T(t) \mathrm{d}t \qquad (20)$$

where U_R, U_J, and U_A are defined in section 2.1. We define the fractional deviation of the integrated energy input $W(P)$ from the integrated output $W(U_T)$ as

$$\text{Deviation from energy sinks} = \frac{W(P)}{W(U_T)} - 1 \qquad (21)$$

For the case of the geomagnetic storm events, we determine the effective area which has the least standard deviation with respect to the events. We find that the deviation from energy sinks for the minor to intermediate storms has best statistics when the effective area $2L_M L_T = 126\,R_E^2$. In Figure 5 we have shown the deviation from energy sinks using $126\,R_E^2$ as the effective area in equation (18). The x axis represents the 1 h averaged B_z magnitude during the maximum solar wind driving for each event. Figure 5 shows that the energy input is underestimated for substorms and overestimated for

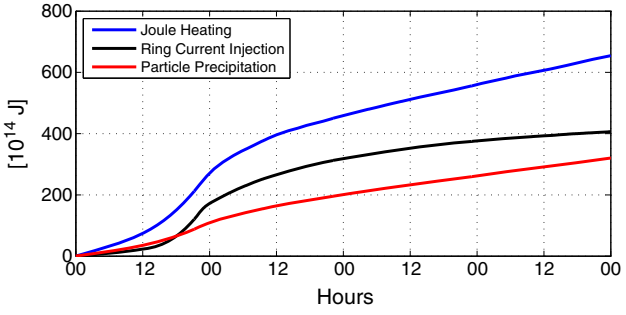

Figure 9. Estimated averaged energy sinks and their contribution to the total during the geomagnetic storm events. The contribution is distributed as follows: Joule heating 47.5%, particle precipitation 23%, and ring current injection 29.5%.

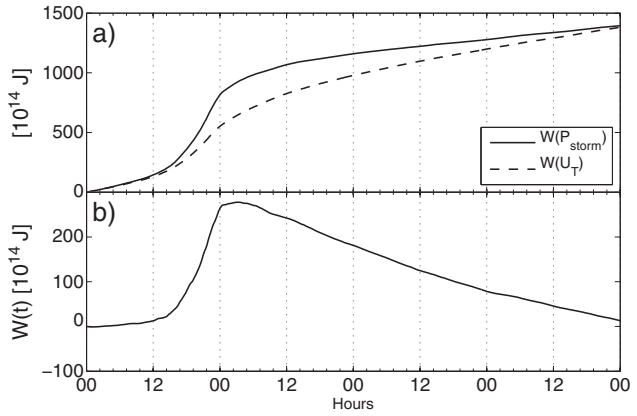

Figure 10. (top) The average integrated energy sinks (dashed line) and energy coupling function (solid). (bottom) The energy budget, $W(t)$, during the averaged geomagnetic storm.

severe storms. We have interpreted this as that the effective area should be considered dynamic, and we have found that the deviation correlates best with the magnitude of the B_z component.

5.4.1. Geomagnetic Storms

[35] We have chosen to represent the dynamic effective area using a power fit with two terms. An algorithm finds the coefficients yielding the best mean and standard deviation of normalized values using the storm events shown in Figure 5.

[36] In Figure 6 we have shown the deviation from energy sinks for each of the 45 geomagnetic storms (of which Events 38–45 are severe storms). The red data points are the calculated deviation using equation (18) with a static effective area ($2L_ML_T$) of 126 R_E^2, while the blue filled points are calculated using a dynamic effective area. The statistics are considerably better for the dynamic (blue) with a standard deviation of 0.13 compared to 0.29 for the static area (red).

[37] The dynamic effective area of interaction found to yield the best statistics is

$$G(B_z) = 2\,L_M\,L_T = \frac{135}{5\times 10^{22}|B_z|^3 + 1} \tag{22}$$

The energy coupling function for geomagnetic storms can then be given as

$$P_{\text{storm}} = \frac{B_T^2 V_x}{\mu_0} M_A \sin^4(\theta/2) \frac{135}{5\times 10^{22}|B_z|^3 + 1} R_E^2 \tag{23}$$

We have defined the coefficient 5×10^{22} to have units T^{-3} in order for the effective area term given in equation (22) to be dimensionless. Also, we emphasize that this term, which represents the area where the energy transfer occurs, is purely empirical and should be considered as a first approximation to an observed effect. How it relates to the dimensional analysis [*Vasyliunas et al.*, 1982] will be discussed.

5.4.2. Long Time Series

[38] When analyzing geomagnetic storms and substorms, it is important to carefully determine the integration period. Still it is likely that for some of the events, the magnetotail stores some of the supplied energy, while for some events, priorly stored energy is released in addition to the energy supplied in the specific event. By looking at sufficiently long periods, we can investigate how the magnetotail distributes the energy. By analyzing several periods ranging from several days to years with consistent solar wind data, we find that the energy coupling function performs best when the effective area of interaction is

$$G(B_z) = 2\,L_M\,L_T = \frac{167}{5\times 10^{22}|B_z|^3 + 1} \tag{24}$$

When considering Figure 5 where the energy transfer was underestimated for the events with $B_z < 10$, it is not surprising that we find that we must increase the effective area. The function $G(B_z)$ describing the dynamic effective area is shown in Figure 7. The energy coupling function applicable for long time periods is then

$$P_{\text{input}} = \frac{B_T^2 V_x}{\mu_0} M_A \sin^4(\theta/2) \frac{167}{5\times 10^{22}|B_z|^3 + 1} R_E^2 \tag{25}$$

Thus, the effective area found for long time series is approximately 20% larger than that for geomagnetic storms. This will be discussed further in section 7.

6. Energy Budget

[39] The energy budget can be established by comparing energy sinks and sources. By assuming a closed system, we try to determine the spatial and temporal evolution of the energy flow through the system. The energy sinks, also called energy output, describe the processes driven by the energy in the system. The energy source, also called energy input, is described by a function depending on solar wind parameters and is a proxy for when and how the magnetosphere couples with the solar wind.

Table 1. The Calculated Time-Integrated Energy Depositions, Energy Coupling Function P_{input}, ϵ Parameter, Total Solar Wind Kinetic Energy U_{SW}, and Coupling Efficiency for Different Periods and Events

Events	$W(U_J)$ [10^{14} J] (%)	$W(U_A)$ [10^{14} J] (%)	$W(U_R)$ [10^{14} J] (%)	$W(U_T)$ [10^{14} J]	$W(P)$ [10^{14} J]	$W(\epsilon)$ [10^{14} J]	$W(U_{SW})$ [10^{14} J]	CE (%)
Substorm	28.5 (54.5)	17.5 (33.5)	6.4 (12)	52.3	48	27	7,898	0.66
Storm[a]	655 (47.5)	320 (23)	406 (29)	1,381	1,394	2,018	1.69×10^5	0.82
20 days	1,394 (54)	878 (34)	299 (12)	2,571	2,582	1,986	4.69×10^5	0.55
4 months	13,800 (55)	7,610 (30)	3,680 (15)	25,150	25,210	18,580	0.386×10^7	0.65
1997	30,300 (52)	19,100 (33)	8,600 (15)	58,000	59,300	35,900	1.04×10^7	0.56
2003	53,200 (54)	27,900 (28)	17,300 (18)	98,400	106,400	94,600	1.64×10^7	0.6
1997–2010	480,000 (54)	270,000 (31)	136,000 (15)	889,000	864,000	668,000	14.9×10^7	0.6

[a]We have used P_{storm} for the energy input during the storm events. Using P_{input} would increase the energy input estimate by approximately 20% to $P_{\text{input}} = 1700 \times 10^{14}$ J.

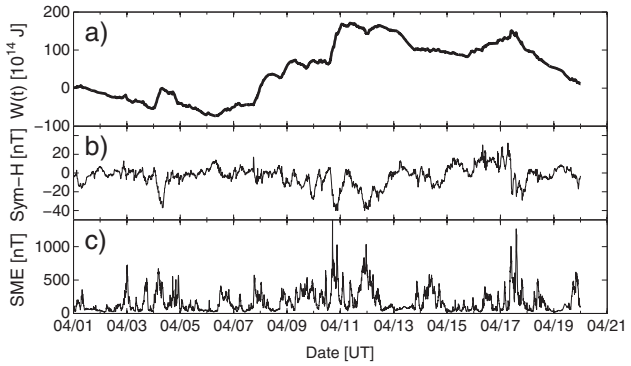

Figure 11. The energy balance calculated using (a) P_{input}, (b) *SYM-H* index, and (c) *SME* index in the period 1 to 21 April 1998. The calculated time-integrated values associated with this event are presented in Table 1.

[40] Such an analysis can help to understand the energy flow in the whole solar wind-magnetosphere-ionosphere system and determine whether the sources and sinks balance in the system.

[41] To calculate the energy balance, we calculate the time-integrated energy input and output as a function of time:

$$W(t) = \int_{t1}^{t2} P(t) - U_T(t)\, dt \tag{26}$$

where $U_T = U_A + U_J + U_R$, and $P(t)$ is the energy coupling function.

6.1. Geomagnetic Storms

[42] We have chosen to use the P_{storm} parameter when presenting the energy balance for geomagnetic storms. Figure 8 shows the available solar wind energy, the energy coupling function P_{storm}, and the energy deposition derived from SuperMAG and Kyoto. The energy sinks, U_J, U_R, and U_A, during the superposed geomagnetic storms give the following contributions to the total (U_T), 47.5%, 29.5%, and 23%, respectively, see Figure 9.

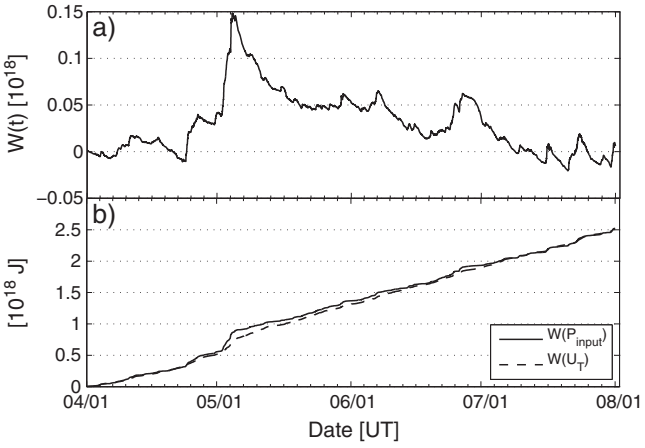

Figure 12. (a) The energy balance calculated and (b) the time-integrated energy coupling function P_{input} and U_T, in the period 1 April to 1 August 1998. The integrated energy input in this period $W(P_{\text{input}}) = 2.5219 \times 10^{18}$ J, the total deposited energy $W(U_T) = 2.5156 \times 10^{18}$ J, and other calculated values are summarized in Table 1.

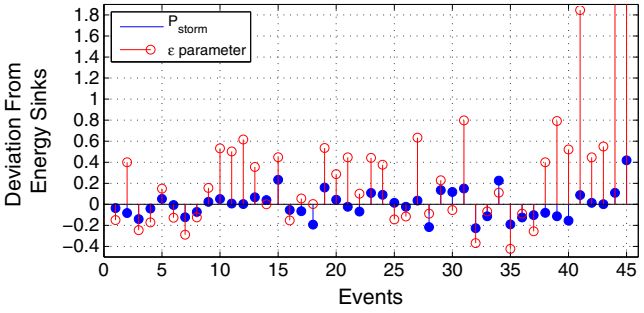

Figure 13. Comparing the deviation from energy sinks for the coupling function P_{storm} (blue) and the ϵ parameter (red) during the geomagnetic storm events.

[43] Figure 10 shows the energy budget during an average geomagnetic storm, calculated using equation (26). The average energy input for the average geomagnetic storm is found to be $W(P_{\text{storm}}) = 0.139 \times 10^{18}$ J, and the time-integrated energy depositions are $W(U_T) = 0.138 \times 10^{18}$ J, see Table 1.

6.2. Long Time Series

[44] When analyzing longer periods, we use P_{input} and will present three different intervals, 20 days, 4 months, and 13 years. The periods analyzed contain both storms and substorms as well as quiet periods with no obvious energy transfer. Figure 11 shows the energy budget, *SYM-H*, and *SME* for a period of 20 days. The purpose of the figure is to show how the energy coupling performs during a relatively quiet period. Still there are several substorms and minor storms; however, the energy coupling function estimates all the events well, as is evident in the energy budget.

[45] In this period, the 0.258×10^{18} J was transferred from the solar wind to the magnetosphere and 0.257×10^{18} J was deposited in the inner magnetosphere and ionosphere. The energy sinks, U_J, U_A, and U_R, during this period give the following contribution to the total ($W(U_T)$): 55%, 33%, and 12%, respectively. These values and more are summarized in Table 1.

[46] Figure 12a shows the energy budget, while Figure 12b shows the time-integrated energy coupling function P_{input} and total energy dissipation U_T during a period of 4 months. In this period, there is a severe geomagnetic storm (occurring 4 May 1998), where the magnitude of IMF B_z reaches values below –35 nT. We observe the huge amount of energy driven into the system during this storm and then dissipated at a somewhat lower rate. The saturation term ($G(B_z)$) in the energy coupling function is crucial for the success of the energy budget during such events. The calculated time-integrated energy input, energy depositions, ϵ parameter, solar wind kinetic energy, and coupling efficiency for this event, as well as for the years 1997 (close to solar minimum) and 2003 (close to solar maximum) are summarized in Table 1.

6.3. Coupling Efficiency

[47] Another important parameter is the coupling efficiency, which is how much of the available solar wind

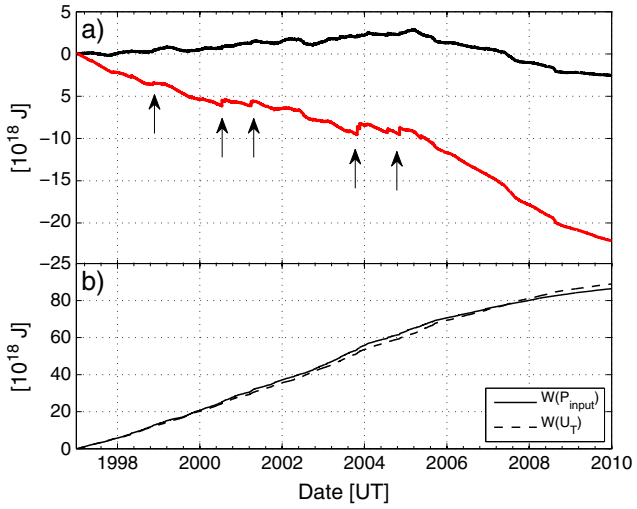

Figure 14. (a) The energy balance, the black line, is calculated using P_{input}, while the red line is the ϵ parameter in the period 1997–2010. The arrows indicate severe storms where the ϵ parameter clearly overestimates the energy input. (b) The integrated energy input and output.

kinetic energy that actually penetrates the magnetosphere. The coupling efficiency is defined as $CE = W(U_T)/W(U_{SW})$. *Østgaard et al.* [2002b] found the coupling efficiency of the solar wind kinetic power to the magnetosphere to be from 0.3 to 0.8%. *Stern* [1984] estimated it to be roughly $\approx$ 1%, while *Lu et al.* [1998] suggest as much as 4%. We note that these results depend on the magnetospheric cross section used. During a geomagnetic storm, we find that *CE* on average is 0.8%, and it reaches values above 1.3% during maximum solar wind driving. For the period 1997–2010, we find the average value of 0.6%. Our results are summarized in Table 1 and are in general agreement with *Østgaard et al.* [2002b] and *Stern* [1984].

6.4. A Comparison With the ϵ Parameter

[48] To our knowledge, as the ϵ parameter is the only energy coupling function scaled to the energy sinks, we find it reasonable to present a comparison. The ϵ parameter was originally determined to analyze geomagnetic storms; for this reason, it should be compared to our P_{storm}. The functional form of the coupling functions is similar yet there are essential differences. P_{storm} uses the x component of the solar wind velocity V_x and the transverse magnetic field component compared to the ϵ parameter's VB. P_{storm} has an Alfvén Mach number dependence, as will be discussed later. Also, we let the effective area of interaction to be dynamic and dependent to the first order on the magnitude of the B_z component. So for all practical reasons, only the angular dependence in the two functional forms is common.

[49] Figure 13 shows the deviation from energy sinks for both P_{storm} and the ϵ parameter for the 45 geomagnetic storm events. On average, the ϵ parameter overestimates the energy input for geomagnetic storms. Especially during the severe storms where it overestimates the energy input by as much as 350% (Event 45 in Figure 13). We note that the ϵ parameter was originally scaled using different estimations of the energy sinks; thus, we should not expect it to perform better. However, it is evident that P_{storm} performs better for the various events and that it handles the relevant properties of the energy input more accurately.

[50] Figure 14 shows how the ϵ parameter performs for long time series and a comparison with the energy coupling function P_{input}. Figure 14a shows the energy balance $W(t)$ (equation (26)), and Figure 14b shows the time-integrated energy coupling function P_{input} and total energy sinks U_T. During this period, the ϵ parameter underestimates the energy input by approximately 33% while P_{input} underestimates by $\approx$ 3%. During this 13 year period, the ϵ parameter underestimates the energy input and should be scaled by a factor of 1.3. However, we note that during the severe storms, identified by the arrows in Figure 14, the ϵ parameter overestimates greatly; thus, it is likely that the scaling factor is somewhat higher during quieter periods.

7. Discussion

[51] In section 2 we mentioned uncertainties related to the estimation of the energy sinks. Regarding Joule heating, there is an ambiguity in the community about how it should be estimated. *Palmroth et al.* [2005] review different methods and techniques and present a comparison of Joule heating estimates from the *Ahn et al.* [1983] proxy, AMIE, Super Dual Auroral Radar Network, Polar satellite measurements, and GUMICS-4. During the event studied, *Palmroth et al.* [2005] argue that the AMIE estimate is too high during peak but consistent with what the authors consider to be the "true" Joule heating toward the end of the substorm. The *Ahn et al.* [1983] proxy is regarded as consistent, however, it is a factor 2 higher during peak. The "true" Joule heating, which is determined using MHD simulations multiplied by a factor of 10, and theoretical arguments coincide well with the global observations [see *Palmroth et al.*, 2005, Table 1] and appear to be less than suggested by, for example, the *AE* proxies [*Palmroth et al.*, 2005]. We acknowledge the uncertainty in the Joule heating estimation using *AE* proxies in this study and that even using the same data the different methods can yield divergent estimates. However, we have used the experimental estimates that in our opinion reflect most accurate the amount of Joule heating dissipated in the ionosphere. Also, we note that in the MHD simulations [*Palmroth et al.*, 2004], both the temporal and spatial variations are well correlated with the empirical proxies, such that it should not affect our correlation analysis significantly. We have used values corresponding to solstice, $U_J = (0.33 + 0.21)AE + 1.8$ (summer + winter) [*Østgaard et al.*, 2002b]. These may differ in the cycle of seasons. *Ahn et al.* [1983] suggested $U_J = 0.23AE$ for one hemisphere during equinox, which we consider reasonable, less than for summer and higher than during winter. Thus, for equinox, Joule heating could be expressed as $U_J = (0.23 + 0.23)AE = 0.46AE$ which represents a deviation of about 15%. The consequence of this uncertainty in the estimated energy sinks will slightly affect the energy coupling function. Even though the functional form will not change, the effective area of interaction will differ. By determining the effective area for geomagnetic storms using an expression for the Joule heating which is scaled $\pm$15%, we find that this results in increase/decrease of about 7% for the effective area. That is,

$$P_{\text{storm}} = \frac{B_T^2 V_x}{\mu_0} M_A \sin^4(\theta/2) \frac{135 \pm 9}{5 \times 10^{22} |B_z|^3 + 1} R_E^2$$

with corresponding percentage uncertainties in P_{input}. Considering the extremes where U_J is off by as much as a factor of 0.5 or 2, this would imply a deviation of the effective area by –30 or +65, respectively. These extremes will be discussed further below. Similarly regarding the particle precipitation, we cannot discard seasonal variations. Our results rely on the study by *Østgaard et al.* [2002b] where the analyzed events occurred during solstice. Compared to previous studies, e.g., the values used by *Akasofu* [1981] only provided $\sim$ 30% of the U_A. As an example, applying an uncertainty of 50% in U_A (equation (6)) will result in a 10% change in the effective area.

[52] For the case of uncertainties in the estimation of the ring current injection rate (equation (9)), the consequence of choosing a dynamic decay rate [*O'Brien and McPherron*, 2000] will affect the scaling. During Event 7 which has a minimum *SYM-H* of about –120 nT, the calculated integrated energy deposition U_R is approximately 40% lower when using the dynamic decay rate. For more severe storms, this would result in an even larger difference, and for weaker storms, the difference would diminish. For this particular storm, the deviation in the effective area in our energy coupling functions would be approximately 6%.

[53] As discussed, it has been proposed that both U_J and U_A could be off by some factor 2. If both these processes were overestimated by a factor of 2, it would imply that U_R is the main dissipation process in the system (at least during storm time): $U_J + U_A \approx U_R$. In this extreme, the functional form should be reconsidered. In the more likely situation where $U_J + U_A > U_R$, our functional form will hold and only the scaling must be changed.

[54] We also would like to comment on the angular dependence, $\sin^{\beta}(\theta/2)$. The exponent value of 4 was chosen based on previous studies [*Gonzalez and Mozer*, 1974; *Akasofu*, 1981; *Kan and Akasofu*, 1982], a correlation analysis where β varied from 0 to 5, and trial and error on different events. The correlation analysis showed that the correlation coefficient did not change significantly for $\beta > 1$. In a trial-based analysis, we considered our 45 geomagnetic storms (see Figure 6) and an algorithm calculated the standard deviation of the 45 events for different values of β. In this case as well, the value of β did not significantly affect the results. The standard deviation improved as β increased, however, only on the second to third decimal. Choosing a higher β value implies a larger effective area in order to balance the energy. Thus, changing the β requires scaling the effective area, and it is possible that these values are dependent. *Gonzalez and Mozer* [1974] discussed how the compression ratio in the magnetosheath could affect the value of β.

[55] We have found two energy coupling functions. P_{storm} is scaled to fit geomagnetic storms, while P_{input} is applicable for long periods. It is well known that the magnetotail stores magnetic energy; therefore, it may not be surprising that these differ. We interpret P_{storm} as the energy directly deposited in the inner magnetosphere and ionosphere [*Rostoker et al.*, 1988; *Baker et al.*, 1997; *Boakes et al.*, 2011]. Comparing P_{input} and P_{storm} would imply that approximately 20% of the transferred energy is stored in the magnetotail during an average geomagnetic storm. The dayside flux rate, Φ_D, could exceed, equal, or be less than the rate of closing flux on the nightside, Φ_N. The former defines how much flux is transported to the tail, while the latter represents how much of the available magnetic flux is transported from the magnetotail to the inner magnetosphere and ionosphere. *Tanskanen et al.* [2005] found that during the substorm expansion phase, Φ_N usually exceeded Φ_D; previously stored flux is then released in addition to the flux which is directly transported.

[56] As previously defined, the effective area of interaction is a product of the geo-effective length, L_M, and the transfer length, L_T. We found that the area is dynamic and varies to the first order on the magnitude of the B_z cubed. In terms of dimensional analysis presented by *Vasyliunas et al.* [1982] (see equation (16)), the fundamental dimensions may only appear in combinations having appropriate dimensions. Thus, in order to be consistent with this analogy, B_z should be multiplied with the inverse dynamic pressure (see equation (17)). This, however, significantly decreased the performance. The part of the coupling function that handles the actual energy transfer/conversion is consistent with the dimensional analysis. However, the effective area representing the area at which the actual energy transfer occurs, rather than the actual energy transfer, is empirical and not consistent with dimensional analysis. We also note that the empirically determined numerical factor 5×10^{22} is very close to the Earth's magnetic dipole moment $M_E = 7.94 \times 10^{22}$ which is probably a coincidence.

[57] Another question arises: How does the area we have estimated correspond to the position of reconnection in the tail? In the magnetosheath, the solar wind is channeled around Earth's magnetosphere, and only a fraction of the solar wind interacts with the magnetopause. The limited extent of the solar wind flow that participates in the dayside reconnection process is the geo-effective length, L_M [*Lopez et al.*, 2011]. *Reiff et al.* [1981] estimated L_M to be roughly 0.1 to 0.2 of the magnetosphere width. More recent studies argued that L_M is in the range of 5–8 R_E, which was later adjusted to $\approx 3\,R_E$ [*Milan*, 2004; *Milan et al.*, 2004, 2008, 2012]. By assuming a merging length of $L_M \approx 3\,R_E$, we can estimate the transfer length L_T to be approximately 28 R_E during a geomagnetic storm. For a severe magnetic storm with an average IMF B_z of $\sim$ 20 nT, L_T would decrease to about 20 R_E. This corresponds well to our assumption that the transfer length is bounded to the position of the tail reconnection [*Nagai et al.*, 2005].

[58] As mentioned in the introduction, we will now discuss how our semiempirical result can be interpreted in view of the Maxwell stress tensor. Considering equation (15), the integral of $B_n V$ can be related to upstream solar wind parameters, and the reconnection rate at the dayside magnetopause is ultimately responsible for the normal component B_n, and thus ultimately the tangential stress. In absence of tangential stress, the magnetopause and tail currents are dissipationless currents on the magnetopause surface; however, when a normal component exists, these currents can influence the flow in the dayside and tail regions, respectively [*Russell*, 2000]. Applying this consideration, we can rewrite equation (15) to $P = \oint B_n \vec{B}_t \cdot \vec{V}/\mu_0 \, d\sigma = V_x B_T L_M \oint dl B_t/\mu_0$ [see *Vasyliunas et al.*, 1982]. In the familiar laws of electric circuit theory, it is evident that P represents the cross-tail electric field times the total current. From our semiempirical coupling function (equation (18)), the total current or the tangential component of the magnetic stress tensor

is given by $\int \mathrm{d}lB_t/\mu_0 = L_T\sqrt{\mu_0 P_f}/\mu_0 = L_T B_T M_A/\mu_0$ [cf. *Akasofu and Perreault*, 1978; *Kan and Lee*, 1979; *Gonzalez and Gonzalez*, 1981; *Vasyliunas et al.*, 1982].

[59] The role of the bow shock in magnetospheric dynamics has generally been unappreciated in the energy coupling between the solar wind and magnetosphere [*Lopez et al.*, 2011]. How the solar wind interacts with the magnetopause is shock dependent [*Lavraud and Borovsky*, 2008]. These properties are Mach number dependent. The coupling occurs at the magnetopause; hence, the characteristics of the magnetosheath properties should be included in the coupling function. It is of our understanding that the Alfvén Mach dependence in the energy coupling function is contributory to capturing the distorted upstream properties of the solar wind in the magnetosheath. The Alfvén Mach number describes the square ratio of kinetic energy flux to the electromagnetic energy flux and reflects, among other things, the position of the bow shock and the amount of compression in the magnetosheath. For the high Mach number regime, the bow shock compression ratio is close to the theoretical maximum of 4 [*Lopez et al.*, 2004]. The Mach number parameter in the energy coupling function will contribute most during such conditions, influencing the energy transfer rate. For the low Mach number regime (magnetosheath is magnetically dominated), the magnetosheath flow is controlled by the Lorentz force, $J \times B$. In this regime, the coupling function dependence on the Mach number acts to saturate the energy input [*Lopez et al.*, 2011; *Lavraud and Borovsky*, 2008]. However, *Lopez et al.* [2004] showed that under these conditions, the compression ratio is strongly dependent on variation in the pressure. Higher density results in larger compression ratio (higher Mach number) resulting in a stronger magnetic field applied to the magnetosphere. The compression ratio also influences the amount of draping, which again could increase the magnetic stress on the magnetopause. We also notice that by using the magnetosheath model by *Crooker et al.* [1979], the magnetosheath field strength can be expressed as $B_{SH} \propto \sqrt{M_A} B_T$. Inserting this in our energy coupling function would then give a functional form similar to the ϵ parameter: $\frac{V_x B_{SH}^2}{\mu_0} \sin^4(\theta/2) 2 L_M L_T$ (if $2 L_T L_M = l_0^2$). Our semiempirical energy coupling function coincides with several arguments on how the magnetosheath behaves during different regimes [*Lopez et al.*, 2004, 2011; *Borovsky*, 2008].

8. Conclusions

[60] In this paper we have presented two new dynamic energy coupling functions, derived using 5 min OMNI and SuperMAG data. The 5 min resolution is considered to be the optimal and characteristic time scale [*Tsyganenko*, 2013]. P_{storm}, derived using 45 geomagnetic storms, is applicable when studying geomagnetic storms but underestimates the energy input for longer time series. It is given as (equation (23))

$$P_{\mathrm{storm}} = \frac{B_T^2 V_x}{\mu_0} M_A \sin^4(\theta/2) \frac{135}{5 \times 10^{22} |B_z|^3 + 1} R_E^2$$

where $B_T = \sqrt{B_y^2 + B_z^2}$ and $M_A = \frac{\sqrt{\mu_0 P_f}}{B_T}$. By studying longer time series ranging from days up to 13 years, we found that the effective area of interaction had to be increased by approximately 20%. The energy coupling function P_{input}, which is applicable for longer time series, is given as (equation (25))

$$P_{\mathrm{input}} = \frac{B_T^2 V_x}{\mu_0} M_A \sin^4(\theta/2) \frac{167}{5 \times 10^{22} |B_z|^3 + 1} R_E^2$$

We have argued that the difference between P_{storm} and P_{input} could be explained by the magnetospheric response to the accumulation of energy in the tail. We also note that defining the geomagnetic storm to have a longer duration would diminish the difference. That is to say that 20% of the energy accumulated in the tail is released subsequently of the defined storm period.

[61] Throughout the paper we have attempted to relate the terms from our semiempirical analysis to theoretical considerations. The Alfvén Mach dependence in our energy coupling function improves the performance of the energy coupling function by increasing the transfer rate for high Mach upstream solar wind and mitigates the energy input during low Mach conditions.

[62] In Table 1 we have listed the time-integrated energy depositions, energy coupling functions P_{input}, P_{storm}, the ϵ parameter, total solar wind kinetic energy U_{SW}, and coupling efficiencies for all the events discussed in the paper. In general, the ϵ parameter underestimates the energy input. This is evident when we look at long time series. Only during geomagnetic storms does the ϵ parameter overestimate the input, but far from enough to compensate for the general underestimate. Thus, for all conditions, we find the dynamic energy coupling function presented in this paper to perform better than ϵ. We believe this new dynamic coupling function can provide new insight to which conditions are more or less favorable for energy transfer and also can be used to study spatiotemporal variations in solar activity, the evolution of energy deposition for long time scales, and how the magnetosheath properties affect the efficiency of the energy transfer among other things.

[63] **Acknowledgments.** This study was funded by Research Council of Norway under contract 223252/F50 to the Birkeland Centre for Space Science as well as contract 216872/F50. We acknowledge the use of NASA/GSFC's Space Physics Data Facility's OMNIWeb service and OMNI data. For the ground magnetometer data, we gratefully acknowledge the following: INTERMAGNET; USGS, Jeffrey J. Love; Danish Meteorological Institute; CARISMA, Ian Mann; CANMOS; the S-RAMP Database, K. Yumoto and K. Shiokawa; the SPIDR database; AARI, Oleg Troshichev; the MACCS program, M. Engebretson, Geomagnetism Unit of the Geological Survey of Canada; GIMA; MEASURE, UCLA IGPP, and Florida Institute of Technology; SAMBA, Eftyhia Zesta; 210 Chain, K. Yumoto; SAMNET, Farideh Honary; the institutes who maintain the IMAGE magnetometer array, Eija Tanskanen; AUTUMN, Martin Conners; Greenland magnetometers operated by DTU Space; South Pole and McMurdo magnetometer, Louis J. Lanzarotti and Alan T. Weatherwax; ICESTAR; RapidMag; PENGUIn; British Antarctic Survey; McMAC, Peter Chi; BGS, Susan Macmillan; Pushkov Institute of Terrestrial Magnetism, Ionosphere and Radio Wave Propagation (IZMIRAN); and SuperMAG, Jesper W. Gjerloev.

[64] Philippa Browning thanks Joseph Borovsky and an anonymous reviewer for their assistance in evaluating this paper.

References

Ahn, B., S. I. Akasofu, and Y. Kamide (1983), The Joule heat production rate and the particle energy injection rate as a function of the geomagnetic indices *AE* and *AL*, *J. Geophys. Res.*, *88*, 6275–6287.

Ahn, B., H. W. Kroehl, Y. Kamide, and D. J. Gorney (1989), Estimation of ionospheric electrodynamic parameters using ionospheric conductance deduced from bremsstrahlung X-ray image data, *J. Geophys. Res.*, *94*, 2565–2586.

Akasofu, S., and P. Perreault (1978), A study of geomagnetic storms, *Geophys. J. R. Astron. Soc.*, *54*, 547–573.

Akasofu, S. I. (1981), Energy coupling between the solar wind and the magnetosphere, *Space Sci. Rev.*, *28*(1963), 121–190.

Anekallu, C. R., M. Palmroth, T. I. Pulkkinen, S. E. Haaland, E. Lucek, and I. Dandouras (2011), Energy conversion at the Earth's magnetopause using single and multispacecraft methods, *J. Geophys. Res.*, *116*, A11204, doi:10.1029/2011JA016783.

Baker, D. N., T. I. Pulkkinen, M. Hesse, and R. L. McPherron (1997), A quantitative assessment of energy storage and release in the Earth's magnetotail, *J. Geophys. Res.*, *102*, 7159–7168.

Barth, C. A., D. N. Baker, and S. M. Bailey (2004), Seasonal variation of auroral electron precipitation, *Geophys. Res. Lett.*, *31*, L04809, doi:10.1029/2003GL018892.

Baumjohann, W., and Y. Kamide (1984), Hemispherical Joule heating and the *AE* indices, *J. Geophys. Res.*, *89*, 383–388.

Boakes, P. D., S. E. Milan, G. A. Abel, M. P. Freeman, G. Chisham, and B. Hubert (2011), A superposed epoch investigation of the relation between magnetospheric solar wind driving and substorm dynamics with geosynchronous particle injection signatures, *J. Geophys. Res.*, *116*, 1–12, doi:10.1029/2010JA016007.

Borovsky, J. E. (2008), The rudiments of a theory of solar wind/magnetosphere coupling derived from first principles, *J. Geophys. Res.*, *113*, 1–14, doi:10.1029/2007JA012646.

Borovsky, J. E., and H. O. Funsten (2003), Role of solar wind turbulence in the coupling of the solar wind to the Earth's magnetosphere, *J. Geophys. Res.*, *108*(A6), 1284, doi:10.1029/2002JA009601.

Burton, R. K., R. L. McPherron, and C. T. Russell (1975), An empirical relationship between interplanetary conditions and *Dst*, *J. Geophys. Res.*, *80*(31), 4204–4214, doi:10.1029/JA080i031p04204.

Crooker, N. U., T. Eastman, and G. Stiles (1979), Observations of plasma depletion in the magnetosheath at the dayside magnetopause, *J. Geophys. Res.*, *84*(A3), 869–874.

Dessler, A. J., and E. N. Parker (1959), Hydromagnetic theory of geomagnetic storms, *J. Geophys. Res.*, *64*(12), 2239–2252.

Dungey, J. W. (1961), Interplanetary magnetic field and auroral zones, *Phys. Rev. Lett.*, *6*(2), 47–48.

Foster, J. C., J.-P. St.-Maurice, and V. J. Abreu (1983), Joule heating at high latitudes, *J. Geophys. Res.*, *88*(A6), 4885–4897, doi:10.1029/JA088iA06p04885.

Gjerloev, J. W. (2012), The SuperMAG data processing technique, *J. Geophys. Res.*, *117*, A09213, doi:10.1029/2012JA017683.

Gonzalez, W. D. (1990), A unified view of solar wind-magnetosphere coupling functions, *Planet. Space Sci.*, *38*(5), 627–632.

Gonzalez, W. D. (1991), Comment On "A tangent subsolar merging line" by N. U. Crooker et al., *J. Geophys. Res.*, *96*, 1873–1874.

Gonzalez, W. D., and A. Gonzalez (1981), Solar wind energy and electric field transfer to the Earth's magnetosphere via magnetopause reconnection, *Geophys. Res. Lett.*, *8*(3), 265–268.

Gonzalez, W. D., and A. Gonzalez (1984), Energy transfer by magnetopause reconnection and the substorm parameter epsilon, *Planet. Space Sci.*, *32*(8), 1007–1012, doi:10.1016/0032-0633(84)90056-4.

Gonzalez, W. D., and F. S. Mozer (1974), A quantitative model for the potential resulting from reconnection with an arbitrary interplanetary magnetic field, *J. Geophys. Res.*, *79*(28), 4186–4194.

Gonzalez, W. D., J. A. Joselyn, Y. Kamide, H. W. Kroehl, G. Rostoker, B. T. Tsurutani, and V. M. Vasyliunas (1994), What is a geomagnetic storm?, *J. Geophys. Res.*, *99*(A4), 5771–5792, doi:10.1029/93JA02867.

Ieda, A., S. Machida, T. Mukai, Y. Saito, T. Yamamoto, A. Nishida, T. Terasawa, and S. Kokubun (1998), Statistical analysis of the plasmoid evolution with Geotail observations, *J. Geophys. Res.*, *103*(A3), 4453–4465, doi:10.1029/97JA03240.

Kallio, E. I., T. I. Pulkkinen, H. E. J. Koskinen, A. Viljanen, J. A. Slavin, and K. Ogilvie (2000), Loading-unloading processes in the nightside ionosphere, *Geophys. Res. Lett.*, *27*(11), 1627–1630.

Kan, J. R., and S. I. Akasofu (1982), Dynamo process governing solar wind-magnetosphere energy coupling, *Planet. Space Sci.*, *30*(4), 367–370, doi:10.1016/0032-0633(82)90042-3.

Kan, J. R., and L. Lee (1979), Energy coupling function and solar wind-magnetosphere dynamo, *Geophys. Res. Lett.*, *6*(7), 577–580.

Kan, J. R., L. Lee, and S. I. Akasofu (1980), The energy coupling function and the power generated by the solar wind-magnetosphere dynamo, *Planet. Space Sci.*, *28*(1974), 823–825.

King, J. H., and N. E. Papitashvili (2005), Solar wind spatial scales in and comparisons of hourly Wind and ACE plasma and magnetic field data, *J. Geophys. Res.*, *110*, 1–9, doi:10.1029/2004JA010649.

Knipp, D. J., et al. (1998), An overview of the early November 1993 geomagnetic storm region which initiated, *J. Geophys. Res.*, *103*(A11), 26,197–26,220.

Koskinen, H. E. J., and E. I. Tanskanen (2002), Magnetospheric energy budget and the epsilon parameter, *J. Geophys. Res.*, *107*, 1–10, doi:10.1029/2002JA009283.

Lavraud, B., and J. E. Borovsky (2008), Altered solar wind-magnetosphere interaction at low Mach numbers: Coronal mass ejections, *J. Geophys. Res.*, *113*, A00B08, doi:10.1029/2008JA013192.

Lopez, R. E., M. Wiltberger, S. Hernandez, and J. G. Lyon (2004), Solar wind density control of energy transfer to the magnetosphere, *Geophys. Res. Lett.*, *31*, L08804, doi:10.1029/2003GL018780.

Lopez, R. E., V. G. Merkin, and J. G. Lyon (2011), The role of the bow shock in solar wind-magnetosphere coupling, *Ann. Geophys.*, *29*, 1129–1135, doi:10.5194/angeo-29-1129-2011.

Lu, G., et al. (1998), Global energy deposition during the January 1997 magnetic cloud event, *J. Geophys. Res.*, *103*(A6), 11,685–11,694.

Milan, S. E. (2004), Dayside and nightside contributions to the cross polar cap potential: Placing an upper limit on a viscous-like interaction, *Ann. Geophys.*, *22*, 3771–3777, doi:10.5194/angeo-22-3771-2004.

Milan, S. E., S. Cowley, M. Lester, D. M. Wright, J. A. Slavin, M. Fillingim, C. W. Carlson, and H. J. Singer (2004), Response of the magnetotail to changes in the open flux content of the magnetosphere, *J. Geophys. Res.*, *109*, 1–16, doi:10.1029/2003JA010350.

Milan, S. E., P. D. Boakes, and B. Hubert (2008), Response of the expanding/contracting polar cap to weak and strong solar wind driving: Implications for substorm onset, *J. Geophys. Res.*, *113*, 1–11, doi:10.1029/2008JA013340.

Milan, S. E., J. S. Gosling, and B. Hubert (2012), Relationship between interplanetary parameters and the magnetopause reconnection rate quantified from observations of the expanding polar cap, *J. Geophys. Res.*, *117*, 1–16, doi:10.1029/2011JA017082.

Nagai, T., M. Fujimoto, R. Nakamura, W. Baumjohann, A. Ieda, I. Shinohara, S. Machida, Y. Saito, and T. Mukai (2005), Solar wind control of the radial distance of the magnetic reconnection site in the magnetotail, *J. Geophys. Res.*, *110*, 1–11, doi:10.1029/2005JA011207.

Newell, P., C. Meng, and K. Lyons (1996), Suppression of discrete aurorae by sunlight, *Nature*, *381*, 766–767.

Newell, P. T., and J. W. Gjerloev (2011a), Evaluation of SuperMAG auroral electrojet indices as indicators of substorms and auroral power, *J. Geophys. Res.*, *116*, A12211, doi:10.1029/2011JA016779.

Newell, P. T., and J. W. Gjerloev (2011b), Substorm and magnetosphere characteristic scales inferred from the SuperMAG auroral electrojet indices, *J. Geophys. Res.*, *116*, A12232, doi:10.1029/2011JA016936.

Newell, P. T., and J. W. Gjerloev (2012), SuperMAG-based partial ring current indices, *J. Geophys. Res.*, *117*, 1–15, doi:10.1029/2012JA017586.

Newell, P. T., T. Sotirelis, K. Liou, C.-I. Meng, and F. J. Rich (2007), A nearly universal solar wind-magnetosphere coupling function inferred from 10 magnetospheric state variables, *J. Geophys. Res.*, *112*, 1–16, doi:10.1029/2006JA012015.

Newell, P. T., T. Sotirelis, K. Liou, and F. J. Rich (2008), Pairs of solar wind-magnetosphere coupling functions: Combining a merging term with a viscous term works best, *J. Geophys. Res.*, *113*, 1–10, doi:10.1029/2007JA012825.

O'Brien, T. P., and R. L. McPherron (2000), An empirical phase space analysis of ring current dynamics: Solar wind control of injection and decay, *J. Geophys. Res.*, *105*(4), 7707–7719.

Østgaard, N., J. Stadsnes, J. Bjordal, G. A. Germany, R. R. Vondrak, G. K. Parks, S. A. Cummer, D. L. Chetnette, and J. G. Pronko (2001), Auroral electron distribution derived from combined UV and X-ray emissions, *J. Geophys. Res.*, *106*, 26,081–26,089.

Østgaard, N., R. R. Vondrak, J. W. Gjerloev, and G. Germany (2002a), A relation between the energy deposition by electron precipitation and geomagnetic indices during substorms, *J. Geophys. Res.*, *107*, 1–7, doi:10.1029/2001JA002003.

Østgaard, N., G. Germany, J. Stadsnes, and R. R. Vondrak (2002b), Energy analysis of substorms based on remote sensing techniques, solar wind measurements, and geomagnetic indices, *J. Geophys. Res.*, *107*, 1233, doi:10.1029/2001JA002002.

Palmroth, M., H. Koskinen, T. Pulkkinen, and P. Janhunen (2004), Ionospheric power consumption in global MHD simulation predicted from solar wind measurements, *IEEE Trans. Plasma Sci.*, *32*, 1511–1518, doi:10.1109/TPS.2004.830989.

Palmroth, M., P. Janhunen, T. I. Pulkkinen, A. Aksnes, G. Lu, N. Østgaard, J. Watermann, G. Reeves, and G. Germany (2005), Assessment of ionospheric Joule heating by GUMICS-4 MHD simulation, AMIE, and satellite-based statistics: Towards a synthesis, *Ann. Geophys.*, *23*, 2051–2068.

Palmroth, M., P. Janhunen, and T. I. Pulkkinen (2006), Hysteresis in solar wind power input to the magnetosphere, *Geophys. Res. Lett.*, *33*, 2–5, doi:10.1029/2005GL025188.

Palmroth, M., H. E. J. Koskinen, T. I. Pulkkinen, P. K. Toivanen, P. Janhunen, S. E. Milan, and M. Lester (2010), Magnetospheric feedback in solar wind energy transfer, *J. Geophys. Res.*, *115*, A00I10, doi:10.1029/2010JA015746.

Parker, E. N. (2007), *Conversations on Electric and Magnetic Fields in the Cosmos*, Princeton Univ. Press, Princeton, N. J. and Oxford, U. K.

Petrinec, S. M., and C. T. Russell (1996), Near-Earth magnetotail shape and size as determined from the magnetopause flaring angle, *J. Geophys. Res.*, *101*(A1), 137–152.

Prigancová, A., and Y. Feldstein (1992), Magnetospheric storm dynamics in terms of energy output rate, *Planet. Space Sci.*, *40*(4), 581–588, doi:10.1016/0032-0633(92)90272-P.

Reiff, P. H., R. W. Spiro, and T. W. Hill (1981), Dependence of polar cap potential drop on interplanetary parameters, *J. Geophys. Res.*, *86*, 7639–7648.

Richmond, A. D., et al. (1990), Global measures of ionospheric electrodynamic activity inferred from incoherent scatter radar and ground magnetometer observations, *J. Geophys. Res.*, *95*, 1061–1071.

Rosenqvist, L., S. Buchert, H. Opgenoorth, A. Vaivads, and G. Lu (2006), Magnetospheric energy budget during huge geomagnetic activity using Cluster and ground-based data, *J. Geophys. Res.*, *111*, 1–14, doi:10.1029/2006JA011608.

Rosenqvist, L., H. J. Opgenoorth, L. Rastaetter, A. Vaivads, I. Dandouras, and S. Buchert (2008), Comparison of local energy conversion estimates from Cluster with global MHD simulations, *Geophys. Res. Lett.*, *35*, 1–6, doi:10.1029/2008GL035854.

Rostoker, G., S.-I. Akasofu, W. Baumjohann, Y. Kamide, and R. L. McPherron (1988), The roles of direct input of energy from the solar wind and unloading of stored magnetotail energy in driving magnetospheric substorms, *Space Sci. Rev.*, *46*, 93–111.

Russell, C. T. (2000), The solar wind interaction with the Earth's magnetosphere: A tutorial, *IEEE Trans. Plasma Sci.*, *28*(6), 1818–1830.

Sckopke, N. (1966), A general relation between the energy of trapped particles and the disturbance field near the Earth, *Geophys. Sci.*, *71*(13), 3125–3130.

Siscoe, G. L. (1972), On the plasma sheet contribution to the force balance requirements in the geomagnetic tail, *J. Geophys. Res.*, *77*(31), 6230–6234.

Siscoe, G. L., and N. U. Crooker (1974), A theoretical relation between *Dst* and the solar wind merging electric field, *Geophys. Res. Lett.*, *1*(1), 17–19.

Siscoe, G. L., and W. D. Cummings (1969), On the cause of geomagnetic bays, *Planet. Space Sci.*, *17*(1963), 1795–1802.

Siscoe, G. L., and K. Siebert (2006), Bimodal nature of solar wind-magnetosphere-ionosphere-thermosphere coupling, *J. Atmos. Sol.-Terr. Phys.*, *68*, 911–920, doi:10.1016/j.jastp.2005.11.012.

Song, P., V. M. Vasyliunas, and X.-Z. Zhou (2009), Magnetosphere-ionosphere/thermosphere coupling: Self-consistent solutions for a one-dimensional stratified ionosphere in three-fluid theory, *J. Geophys. Res.*, *114*, A08213, doi:10.1029/2008JA013629.

Sonnerup, B. U. O. (1974), Magnetopause reconnection rate, *J. Geophys. Res.*, *79*(10), 1546–1549.

Stamper, R., M. Lockwood, M. N. Wild, and T. Clark (1999), Solar causes of the long-term increase in geomagnetic activity, *J. Geophys. Res.*, *104*(12), 28,325–28,342.

Stern, D. P. (1984), Energetics of the magnetosphere, *Space Sci. Rev.*, *39*(1-2), 193–213, doi:10.1007/BF00173674.

Tanskanen, E. I., T. I. Pulkkinen, and H. E. J. Koskinen (2002), Substorm energy budget during low and high solar activity: 1997 and 1999 compared, *J. Geophys. Res.*, *107*, 1086, doi:10.1029/2001JA900153.

Tanskanen, E. I., J. A. Slavin, D. H. Fairfield, D. G. Sibeck, J. W. Gjerloev, T. Mukai, A. Ieda, and T. Nagai (2005), Magnetotail response to prolonged southward IMF *Bz* intervals: Loading, unloading, and continuous magnetospheric dissipation, *J. Geophys. Res.*, *110*, 1–16, doi:10.1029/2004JA010561.

Tsyganenko, N. (2013), Data-based mapping of our dynamical magnetosphere (Julius Bartels Medal lecture), *Geophys. Res. Abst.*, *15*, EGU2013-13184-2.

Turner, N. E., W. D. Cramer, S. K. Earles, and B. A. Emery (2009), Geoefficiency and energy partitioning in CIR-driven and CME-driven storms, *J. Atmos. Sol.-Terr. Phys.*, *71*, 1023–1031, doi:10.1016/j.jastp.2009.02.005.

Vasyliunas, V. M. (2005), Meaning of ionospheric Joule heating, *J. Geophys. Res.*, *110*, A02301, doi:10.1029/2004JA010615.

Vasyliunas, V. M., J. R. Kan, G. L. Siscoe, and S. I. Akasofu (1982), Scaling relations governing magnetospheric energy transfer, *Planet. Space Sci.*, *30*(4), 359–365.

Wanliss, J. A., and K. M. Showalter (2006), High-resolution global storm index: *Dst* versus *SYM-H*, *J. Geophys. Res.*, *111*, A02202, doi:10.1029/2005JA011034.

Weimer, D. R., D. Ober, N. C. Maynard, M. Collier, D. J. McComas, N. Ness, C. W. Smith, and J. Watermann (2003), Predicting interplanetary magnetic field (IMF) propagation delay times using the minimum variance technique, *J. Geophys. Res.*, *108*(A1), 1–12, doi:10.1029/2002JA009405.

Yeh, T., J. R. Kan, and S. I. Akasofu (1981), A theoretically derived energy coupling function for the magnetosphere, *Planet. Space Sci.*, *29*(4), 425–429.